Near-Infrared Tunable Surface Lattice Induced Transparency in a Plasmonic Metasurface

Lior Michaeli, Haim Suchowski, and Tal Ellenbogen*

Collective coherent scattering at the surface of a plasmonic nanoparticle array is shown to induce tunable transparency windows at the localized plasmon band. Broadband phase measurements show that the enhanced transmission is accompanied by a large anomalous dispersion, which leads to a group delay as large as ∼8 fs within only 40 nm thick sample. This effect occurs over a wide tunable spectral range of ∼200 nm, and appears for two distinct counter-propagating surface waves. The experimental observations are in good agreement with calculations based on coupled dipole approximation (CDA) and with finite-difference time-domain (FDTD) simulations. This study opens the door for implementation in the fields of sensing, displays, optical buffering, tunable filtering, and nonlinear optics.

1. Introduction

Coherent scattering of light serves the basis to various optical phenomena, such as openings of optical bandgaps in photonic crystals,[1] quasi-phase-matching of nonlinear optical processes,[2] and the century-old Rayleigh anomaly (RA).[3] Recently it was shown that in ordered arrays of nanoparticles, the coherent buildup of scattered light at the array plane can significantly alter the collective optical response. In the case of metallic nanoparticles, where localized surface plasmon resonances (LSPRs) dictate the absorption and scattering behavior, the simultaneous existence of LSPR with coherently scattered light at the surface of the array can lead to hybridized photonic-plasmonic resonances, known as surface lattice resonances (SLRs).[4–6] These unique resonances have attracted much attention over the last decade. It was shown that the narrow spectral features that accompany the SLRs, along with their photonic

L. Michaeli, Prof. T. Ellenbogen
Department of Physical Electronics
Faculty of Engineering
Tel Aviv University
Tel Aviv 6779801, Israel
E-mail: liormic1@mail.tau.ac.il
L. Michaeli, Prof. H. Suchowski
Raymond and Beverly Sackler School of Physics & Astronomy
Tel Aviv University
Tel Aviv 6779801, Israel
L. Michaeli, Prof. H. Suchowski, Prof. T. Ellenbogen
Center for Light-Matter Interaction
Tel Aviv University
Tel Aviv 6779801, Israel

The ORCID identification number(s) for the author(s) of this article can be found under https://doi.org/10.1002/lpor.201900204

bandgaps behavior, make them attractive to various potential processes and applications, such as Bose–Einstein condensation at room temperature,[7] enhanced nonlinearity,[8] lasing,[9] and sensing.[10]

Electromagnetically induced-transparency (EIT), which is a quantum coherent effect induced by strong interaction with a three-level resonant atomic media,[11] has recently found its counterpart in micro- and nanostructured optical materials.[12–20] This phenomenon, so called EIT-like effect, emerges due to the coupling of superradiant and subradiant modes of the system. The enhanced transmission is accompanied by enhanced group delay of the light, which altogether may pave the way toward implementation of on-chip optical signal processing in the time domain and enhanced linear and nonlinear light–matter interactions. To date, most of the experimental demonstrations of EIT-like effects in metallic micro- and nanostructures rely on the coexistence of two bright and dark localized modes, which, by near-field coupling, cause drastic reduction of the bright mode extinction.[12–14,21,22] Alternative approach to obtain EIT-like effect using plasmonics is by introducing delocalized modes into the system and relying on the destructive interference of either distributed-distributed modes or localized-distributed modes. The first mechanism, which resembles the origin of slow light near the band-edge of photonic crystals, was suggested and demonstrated in various schemes at different spectral ranges.[23–25] Early demonstration of the second mechanism was done by Linden et al.,[26] who showed suppression of extinction in a system composed of plasmonic array above a dielectric substrate that supports guided modes. Following this demonstration, the approach of relying on coupling between localized resonances and distributed waveguide modes has been proposed in several configurations.[27–31] Nevertheless, hardly any experiment has studied the interesting effect of slow light induced by surface lattice resonances, nor have shown spectral tunability of the transparency window. Recently two groups have also studied lattice induced transparencies in the THz spectral range,[32–34] where high transparency values and large group delays were obtained at normal incidence for specific operation frequency. Yet, in the optical range such studies have not been performed to date.

Here we experimentally demonstrate the formation of a near-infrared, spectrally tunable, narrow transparency window within a plasmonic absorptive band of split-ring resonators (SRRs) based metasurface. We experimentally show that the enhanced transmission is accompanied with high anomalous dispersion

which leads to group delay as large as ∼8 fs within only 40 nm thick sample. These experimental measurements are validated by finite-difference time-domain (FDTD) simulations. Moreover, we use the coupled dipole approximation (CDA) to obtain further insight on the nonlocal coupling dynamics in the system. Our analysis reveals that the intriguing effect of strong absorption-less interaction on the resonant plasmonic metasurface is attributed to a special case of photonic–plasmonic hybridization. We find that exactly when coherent scattering of light at the array plane occurs, that is, at the RA condition, equal magnitudes and opposite phases of the incident and scattered light leads to full electric-field cancelation at the nanoparticles' positions. The observed effects occur for two distinct counter-propagating surface waves and show tunability of the EIT-like behavior over a wide spectral range of ∼200 nm. Interestingly, these effects occur only for S-polarized light, which therefore may render this phenomenon the complementary metamaterial behavior of the conventional Brewster angle.

2. Results and Discussion

2.1. Absorption-Less Band Predicted by the Coupled Dipole Approximation

To investigate the collective effects that lead to the appearance of SLR induced EIT-like phenomena we use the CDA. This simplified model captures the core physics behind the studied multi-particle coupling mechanism, and is able to predict and reproduce phenomenologically various related observations.[4,8,10,35–39] The CDA takes into account the inter-particle scattering, and aims to find the effective polarizability, α_{eff}, of each individual particle. The resulting α_{eff} depends on the single particle polarizability α_s, the array geometry, the angular frequency of light ω, the refractive index of the ambient medium $n(\lambda)$, and the angle of incidence θ. In the case of a finite array, a set of linear equations needs to be solved to obtain each particle's effective polarizability,[35,36] while for infinite array, as we consider here, a simple and insightful expression can be derived[40]

$$\alpha_{\text{eff}} = \frac{1}{1/\alpha_s - S\left(\vec{k}_{||}\right)} \tag{1}$$

where $S(\vec{k}_{||}) = \sum_{j \neq i} A_{ij} \cdot e^{-i\vec{k}_{||} \cdot \vec{r}_j}$ is the array's incident angle-dependent structural factor, A_{ij} is the dipole Green function, $\vec{k}_{||}$ is the parallel to the surface component of the incident wavevector $\vec{k} = [2\pi \cdot n(\lambda)/\lambda] \, \hat{k}$ and $\vec{r}_j$ is the location of the jth particle. The structural factor $S(\vec{k}_{||})$ has peaks in its magnitude when there is a coherent buildup of its terms, that is, at the RAs condition: $\vec{k}_{||} + \vec{G}_{m_1,m_2} = \vec{k}_s$, where $\vec{G}_{m_1,m_2} = m_1\vec{b}_1 + m_2\vec{b}_2$ is a general reciprocal lattice vector that is a linear combination of the primitive lattice vectors, and $\vec{k}_s = |\vec{k}|\hat{k}_s$ is the surface scattered wave. The vectors $\hat{k}$ and $\hat{k}_s$ are unity vectors specifying the directions of the incident and scattered surface wavevectors, respectively. From the expression in Equation (1) it can be seen that a

resonant response of α_{eff}, due to the plasmonic and photonic modes reflected by α_s and S respectively, can be determined by $\Delta \equiv \Re\{1/\alpha_s - S\}$, with dissipation determined by $\Gamma \equiv \Im\{1/\alpha_s - S\}$. These resonances of α_{eff}, known as SLRs, occur due to diffractive coupling of the particles at the array. Thackray et al.[10] have pointed out that two types of SLRs can be distinguished; Type 1: occurs when the minimum of Δ is positive and then a single narrow Fano-type resonance appears at the RA condition. Type 2: occurs when the minimum of Δ is negative, and then the curve of $\Re\{1/\alpha_s\}$ intersects twice the curve of $\Re\{S\}$. At this case two unequal collective resonances of α_{eff} are observed, while in between these resonances, at the RA, reduced extinction gap may form.[10] It was found that for 1D chains, one of the two resonances is strongly damped,[4,10] which may affect the quality of the reduced extinction gap. While, as we show here, in 2D arrays this strong damping is significantly diminished. If the gap in-between the two resonances is narrow and deep enough, the Kramers–Kronig relations can be used to show that it is associated with a large negative dispersion and thus enhanced group delay.[41,42] Therefore, as we show here, type 2 SLRs on 2D arrays have the potential for the realization of EIT-like and slow-light behavior.

To investigate the formation of EIT-like features in the system, we use the CDA and analyze the optical response of the array for four different cases presented in **Figure 1**. For each case we examine the interplay beetween α_s and S, and its associated influence on the collective optical extinction. We take the single particle polarizability to be a Lorentzian of the form $\alpha_s = A_0/(\omega_0^2 - \omega^2 + i\gamma\omega)$ with amplitude $A_0 = 5.2 \times 10^{14}$ cm³s⁻², resonance angular frequency $\omega_0 = 2\pi c/\lambda_0$, resonance free space wavelength $\lambda_0 = 868$ nm, angular frequency $\omega = 2\pi c/\lambda$, where c is the speed of light, and damping constant $\gamma = 382$THz. The damping constant here accounts for both radiative and non-radiative losses. The ambient medium refractive index is taken to be $n = 1.51$, and the array x- and y-spacings are $d_x = 270$ nm and $d_y = 800$ nm, respectively. The angle of incidence is set to be $\theta = 26°$, so that the ⟨0, −2⟩ RA condition will ocur at $\lambda_{\langle 0,-2 \rangle}^{RA} \approx 869$ nm, and therefore will coincide with the LSPR centered around λ_0.

In Figure 1a–c, we use the above parameters to calculate the response of a 1D particle chain arranged along the y-direction (with spacing $d_y = 800$ nm). The extinction cross section of each particle in the array is calculated by $\sigma_{\text{ext}} = 4\pi k \cdot \Im\{\alpha_{\text{eff}}\}$. For convenience we present the normalized extinction $C_{\text{ext}} = \sigma_{\text{ext}}/\sigma_0$ where $\sigma_0 = d_x d_y \cos(\theta)$ is the angle-dependent area of a unit cell, and d_x and d_y are the array x- and y-spacing. We note that for the normalization purposes we take $d_x = 270$ nm also for the 1D chain. In Figure 1a,b the real and imaginary parts of S and α_s are plotted, respectively. The difference between these quantities correspond to Δ and Γ defined above. It can be seen that the real part of S has a peak at the ⟨0, −2⟩ RA. In the vicinity of this RA there is a single intersection of the real parts, that is, $\Delta = 0$, determining the spectral location of the hybridized new resonance, and a step-like shape of the difference of imaginary parts Γ, leading to abrupt enhancement of the extinction at longer wavelengths than the RA point, as seen in Figure 1c. Overall, the extincion lineshape for the 1D chain shows very limited reduced extinction gap at the RA.
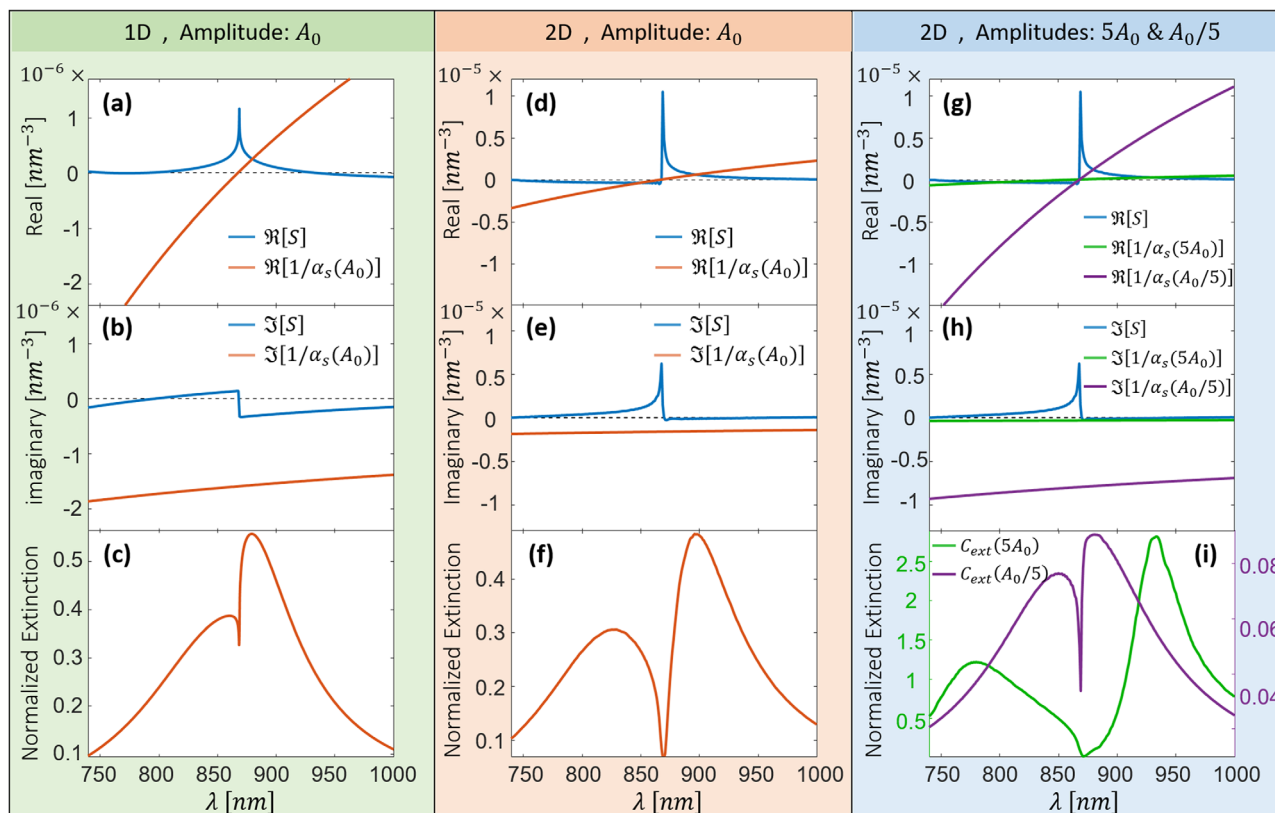
**ADVANCED
SCIENCE NEWS**
www.advancedsciencenews.com

LASER
&PHOTONICS
REVIEWS

www.lpr-journal.org

Figure 1. The interplay between the single particle and the whole array response, and their influence on the spectral extinction. The first column a–c) shows the real (a) and imaginary (b) parts of $1/\alpha_s$ and S, and the normalized extinction (c) of a 1D array with parameters given in the text. d–f) show the same quantities as in (a–c), but for a 2D array. The absorption-less band around $\lambda^{RA}_{\langle 0,-2\rangle} \approx 869$ nm shows narrower and deeper lineshape. g–i) show calculations for a 2D array with fivefold enhanced (green) and fivefold reduced (purple) amplitude of α_s. In both cases, the extinction (i) shows deviation from the desired lineshape of EIT, as presented in (f).

In Figure 1d–f we show similar plots to those shown in Figure 1a–c, but for a 2D array with the same periodicity in the y-direction and subwavelength periodicity in the x-direction ($d_x = 270$ nm and $d_y = 800$ nm). In this case, the peak of the real part of S rises much higher due to the addition of particles participating in the coherent scattering (notice the change in the y-axis range), which dictates a larger Δ and therefore reduced extinction at the RA. At both sides of the RA the real parts of S and $1/\alpha_s$ show intersections, which leads to resonative behavior surrounding the reduced extinction at the RA. In addition, from Figure 1e we see that now the imaginary part of S shows more symmetric lineshape around the RA, which leads to two distinct resonances, with a spectral hole burned in-between them. We stress that this absorption-less band appears while taking the entire loss mechanisms into account.

Next, we show that this desired behavior of the extinction that resembles the EIT lineshape, is strongly dependent on the amplitude of the polarizability, which in turn, commonly varies with the nanoparticles volume. Figure 1g–i show calculations for a 2D array with the same parameters as before, for two different amplitudes of α_s: $5A_0$ and $A_0/5$. While S has not changed from the calculations at Figures 1d–f the change in $1/\alpha_s$ is clearly seen: α_s has a constant resonance wavelength of $\lambda_0 = 868$ nm in all the calculated cases, therefore $\Re\{1/\alpha_s\}$ vanishes at this wavelength. The

change in A_0 causes tilt of the curve describing $\Re\{1/\alpha_s\}$, which in turn sets the crossing points with $\Re\{S\}$ at more separated locations as A_0 increases. In addition, the imaginary parts shown in Figure 1h set smaller Γ as A_0 increases. Therefore, the extinction (Figure 1i) reaches greater values as the amplitude A_0 increases, followed also by larger coupling of the plasmonic and photonic modes, that is, larger spectral separation of the resonances. On the other hand, when A_0 decreases reduced extinction along with smaller resonance splitting is observed. To obtain EIT-like behavior we wish to have large extinction values and a sharp dip between two peaks. Thus, Figure 1f shows the desired behavior of the extinction, while the results in Figure 1i for either the reduced or enhanced polarizability amplitude deviate from the desired trend. Hence, in the following we use the parameters used for the extinction calculation in Figure 1f.

2.2. Anomalous Phase Behavior Predicted by the Coupled Dipole Approximation

The spectral features obtained from the simulated array (see Figure 1d–f) were further studied to obtain the spectral phase response, for normal and for oblique incidence. **Figure 2**a presents the normalized extinction at normal incidence and at

**ADVANCED
SCIENCE NEWS**
www.advancedsciencenews.com
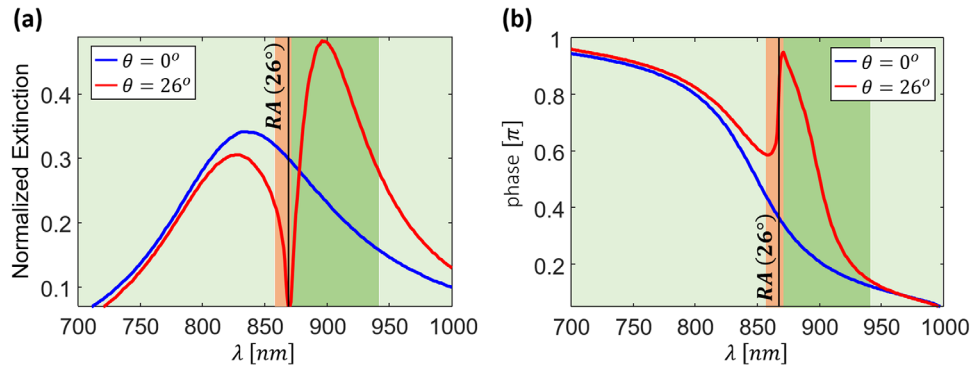
LASER
& PHOTONICS
REVIEWS

www.lpr-journal.org

Figure 2. Absorption-less band accompanied by anomalous phase behavior. a) Simulated normalized extinction for two angles of incidence: $\theta = 0°$ (blue line) and $\theta = 26°$ (red line). b) The phase associated with the extinction of (a), calculated by the Kramers–Kronig relations on a finite bandwidth. The bright-green, dark-green, and orange regions in (a) and (b) correspond to regions with small positive, large positive, and large negative $d\phi/d\omega$ values.

oblique incidence of $\theta = 26°$. The extinction of the oblique incidence is equivalent to that shown in Figure 1f and formerly discussed, while the extinction for normal incidence shows broad resonance that origins mainly from each particle's LSPR. The last remark is confirmed by the observations in Figure 1 that $S \approx 0$ far from any RA, which implies using Equation (1) that $\alpha_{\text{eff}} \approx \alpha_s$. By using the Kramers–Kronig relations, the frequency-dependent phase behavior can be calculated from the frequency-dependent absorption. In Figure 2b we show the corresponding phase calculated by the Kramers–Kronig relations on a finite bandwidth. The changing phase slopes shown in Figure 2b, according to $d\phi/d\omega$, can help distinguish between three different regions that are marked with different colors in Figure 2a,b. Bright green, dark green, and orange regions mark small positive, large positive, and large negative $d\phi/d\omega$ values, respectively. As elaborated in Section 2.4, the large negative $d\phi/d\omega$ region, right around the RA and absorption-less band, implies slow-light behavior.

2.3. SLR Induced Transparency—Experiments and Simulations

To experimentally examine the EIT features studied by the CDA we fabricated a corresponding metasurface comprising gold SRRs. These types of metasurfaces were studied extensively during the last two decades, mainly due to their engineered magnetic response,[43–45] and artificial enhanced and controllable quadratic nonlinearities.[8,46–50] Therefore, showing EIT-like behavior and slow light effects in SRR based metasurfaces may further allow controlling their associated phenomena. The sample, consisting of a 50 μm × 50 μm rectangular array of gold SRRs, was fabricated by a standard electron-beam lithography. The array x- and y-spacing was $d_x = 270$ nm and $d_y = 800$ nm, respectively (**Figure 3**a), which support the existence of RAs only along the y-direction. Each SRR had 190 nm base-length, 225 nm arms-length, 55 nm arms-width, 95 nm base-width, and thickness of 40 nm (Figure 3b). The sample was covered by immersion oil ($n = 1.51$), to obtain symmetric refractive index environment, and was placed on a rotational stage (Figure 3c,d). A white-light source (SuperK COMPACT, NKT Photonics) spanning wavelengths between 450 and 2400 nm was used (Figure 3d) to shine

x-polarized light on the sample (parallel to the base of the SRRs). Only the zero-order transmitted light was collected by an objective and tube lens and spectrally measured by an imaging spectrometer, allowing also broadband interferometric phase measurements by addition of a double-hole mask (for details see Section S1, Supporting Information).

We present the normalized extinction spectra of the studied sample in **Figure 4**a for two angles of incidence, $\theta = 0°$ (blue line) and $\theta = 26°$ (red line). These extinctions were calculated from the measured zero-order transmission $T_{\langle 0,0 \rangle}$ by $C_{\text{ext}} = 1 - T_{\langle 0,0 \rangle}$. The resonance that corresponds to the normal incidence case, originates from the particle's LSPR,[51] as discussed in Section 2.2 (for full resonance characterization see Section S2, Supporting Information). It can be seen that the experiment supports narrow absorption-less band at the RA location, in agreement with the CDA simulation results in Figure 2a. Therefore, one may expect different regions of phase behavior as shown in Figure 2a,b. The region of large expected negative $d\phi/d\omega$ values is marked in Figure 4a by the orange background color. Furthermore, it is also expected that the spectral location of the LSPR would stay approximately constant with varying angle of incidence, whereas the dispersive RA will follow $\lambda^{RA}_{\langle 0, m_y \rangle} = \frac{n(\lambda) \cdot d_y}{|m_y|} (1 - \text{sign}(m_y) \cdot \sin(\theta))$, where m_y is an integer indicating the yth spatial diffraction order. Therefore, it is insightful to examine the plasmonic–photonic coupling, responsible for the observed effect, for varying incident angles. To do that we show the measured (Figure 4b) and simulated (Figure 4c) zero-order transmission for $\theta \in [0°, 30°]$ through the array. Figure 4c shows $T_{\langle 0,0 \rangle}$ obtained by a FDTD solver (Lumerical). In these simulations the physical dimensions of the SRRs were slightly optimized relative to the fabricated sample to get similar spectral response to the measurements (see Section S3, Supporting Information). In Figure 4d we show the transmission simulated by the CDA, calculated by $1 - C_{\text{ext}}$. It can be seen that the measurements agree well with the FDTD simulation results and with the CDA calculations. The deviation of the CDA calculations in Figure 4d for wavelengths smaller than ∼700 nm occurs due to the existence of higher order LSPR centered at wavelength of ∼550 nm which was not taken into account in our CDA model. The agreement between simulations and measurements over the
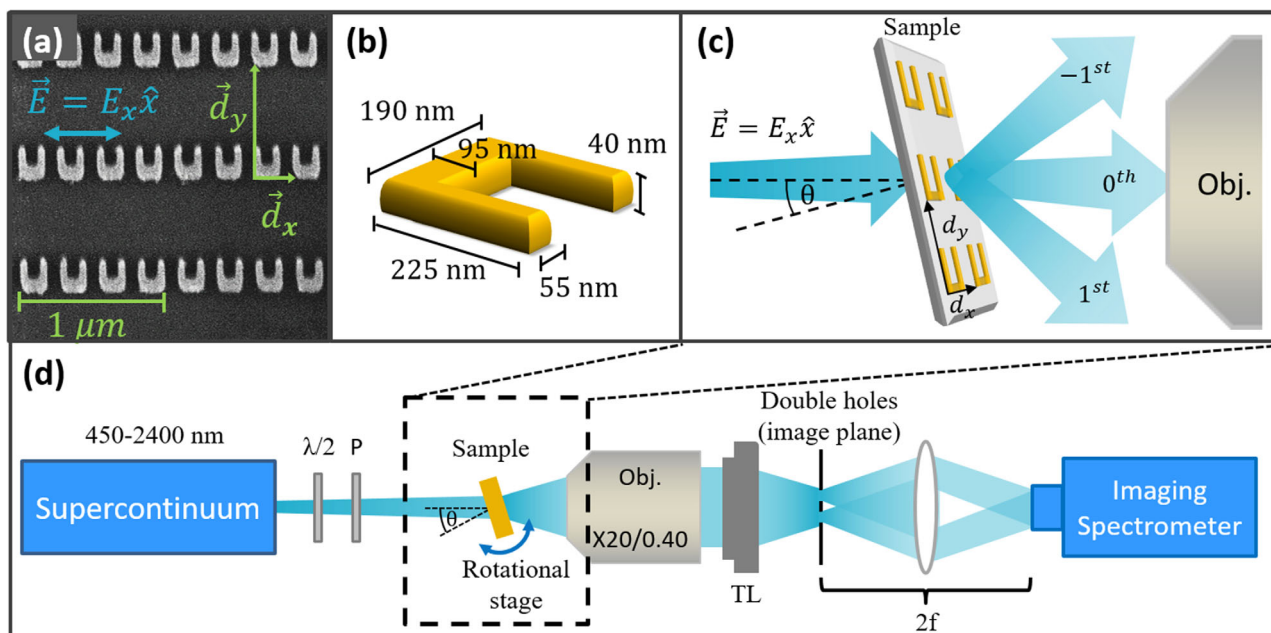
ADVANCED
SCIENCE NEWS
www.advancedsciencenews.com

LASER
&PHOTONICS
REVIEWS

www.lpr-journal.org

Figure 3. Metasurface information and experimental apparatus. a) Scanning electron microscope image of the fabricated sample. The incident electric field polarization is shown with the blue arrow. b) Illustration of the physical dimensions of each SRR. c) Illustration of the sample illumination and transmitted light collection. The incident light was *x*-polarized (parallel to the base of the SRRs), at an angle θ pivoting the *x*-direction. Only the zero-order transmitted light was collected by the objective. d) The experimental setup for the transmission and phase measurements. The setup comprised a supercontinuum source, half-wave plate ($\lambda/2$), polarizer (P), sample on a rotational stage, objective lens (Obj.), tube lens (TL), double-hole mask, 2f system, and an imaging spectrometer.

relevant region of interest (above ∼700 nm) allows us to further investigate the observation with the FDTD and CDA simulations.

In the results, two different RAs, with an opposite slope in the wavelength (*x*-axis) -angle (*y*-axis) map can be distinguished. These RAs correspond to coherent buildup of scattered fields along opposite directions on the array. The $\langle 0, 1 \rangle$ (white dots) and the $\langle 0, -2 \rangle$ (black dots) RAs are co-directed and counter-directed with the parallel to the surface component of the incident wavevector, respectively. Narrow transparency windows appear at these two RAs, resulting in the formation of three separate absorption bands: i) A nondispersive band centered at ∼845 nm for $\theta \in [0°, 15°]$. ii) Concaved shaped band centered at ∼910 nm for $\theta \in [10°, 30°]$. iii) Another nondispersive band centered at ∼845 nm for $\theta \in [22°, 30°]$. At the crossing region of the two RAs a non-dispersive reduced transmission gap is seen, in agreement with previous observations of bandgap formation at the simultaneous coexistence of two RAs.[52,53]

2.4. SLR Induced Slow Light—Experiment and Simulations

To investigate the expected slow light associated with the transparency windows we further measured and simulated the spectral phase of the zero-order transmitted light. The interferometric phase measurements were performed in common-path off-axis geometry and allowed us by a single capture to acquire the phase of the entire spectral range of interest, for each angle (for details see Section S1, Supporting Information). In **Figure 5**a we show the measured spectral phase for varying angles of incidence. Ex-

amining the phase at the array resonances, in accordance to their previous classification, a typical lineshape associated with a phase of Lorentzian is evident for absorption band i) while looking at the two other bands, ii) and iii) more complex phase variations can be seen, indicating the hybridized nature of these resonances. Importantly, we find that at the transparency along the RAs there is an abrupt phase change, as the Kramers–Kronig relations applied to Figure 2a imply. This phase dispersion, $\phi(\omega)$, quantifies the phase accumulated for each frequency component due to the interaction with the metasurface, and can be used directly to calculate the group delay $\tau_g = -\frac{d\phi}{d\omega}$. In Figure 5b,c we show the group delay extracted from the experiment (Figure 5b) and from FDTD simulation (Figure 5c). The experimental measurements and simulations show good agreement. At the RAs, mainly above their cross-point, the light is substantially delayed by the sample, reaching delay values of $\tau \approx 8$ fs, caused by the 40 nm thick sample. This delay occurs, both at the $\langle 0, 1 \rangle$ (white dots) and the $\langle 0, -2 \rangle$ (black dots) RAs, exactly at the transparency windows. In Figure 5d we show a cross section of the group delay (blue line) and the associated transmission (orange line) for $\theta = 26°$. The high transmission peak ($T \approx 92\%$, Q factor ≈ 40) coincides with the high group delay peak (∼7 fs). To elucidate the values shown for τ_g, which quantifies the delay of a pulse traversing the medium, it is worth comparing it with the time it takes to the pulse to cross the same width of the sample in free space. This time is $\tau \approx 40 \frac{\text{nm}}{c} \approx 0.13$ fs. Their ratio, τ_g / τ, which may be viewed as an effective group index, reaches values on the order of ∼60 along the RAs. These findings imply that the time the light interacts with the sample is considerably longer than it would cross the same thickness at the speed of light, and yet, among the
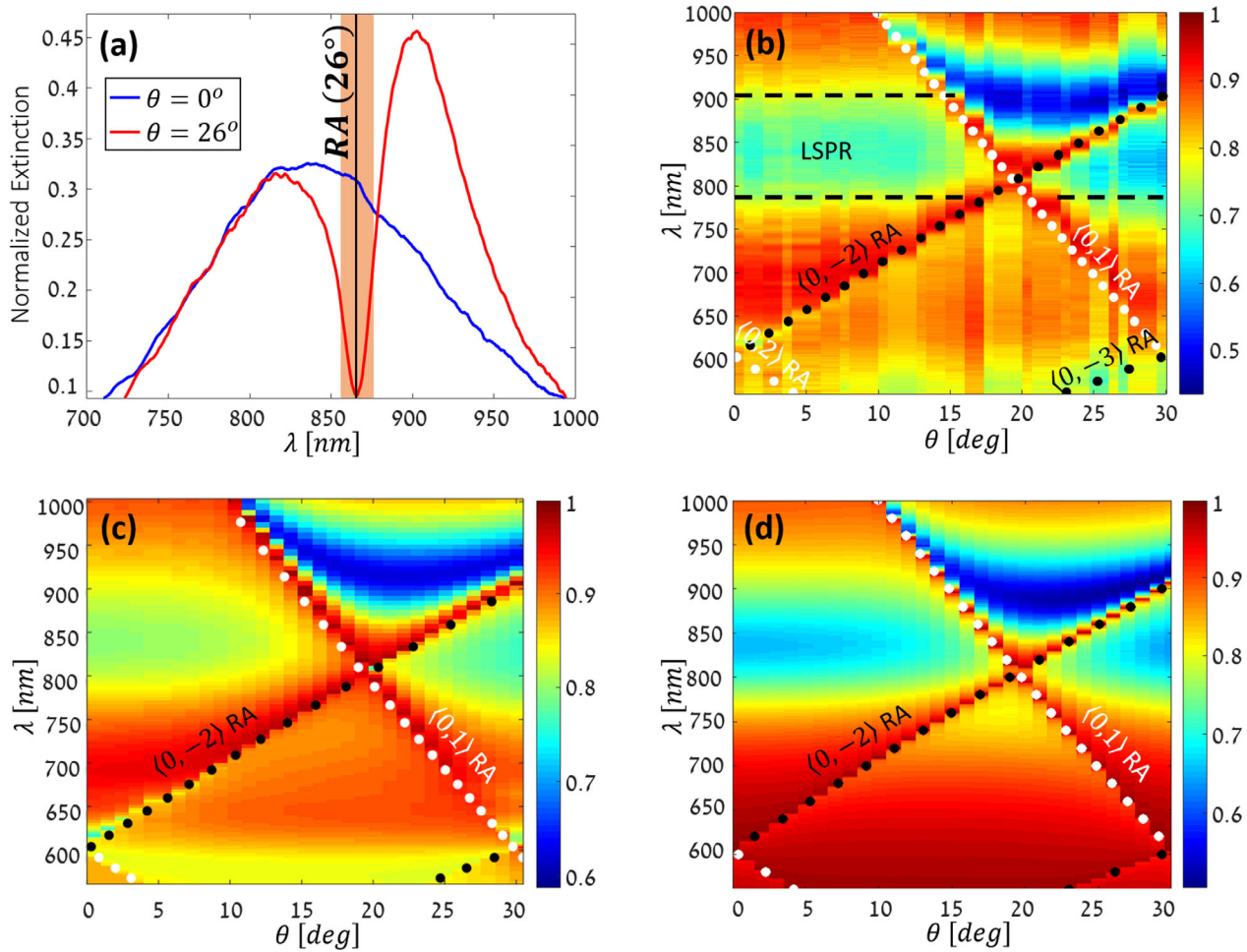
**ADVANCED
SCIENCE NEWS**

www.advancedsciencenews.com

LASER
& PHOTONICS
REVIEWS

www.lpr-journal.org

Figure 4. SLRs induced transparency. a) Experimental x-polarized normalized extinction for two angles of incidence: $\theta = 0°$ (blue line) and $\theta = 26°$ (red line). b) Experimental and c) FDTD simulated zero-order transmission for $\theta \in [0°, 30°]$. d) Shows $1 - C_{ext}$ simulated by the CDA. In (b–d) the $\langle 0, 1 \rangle$ and $\langle 0 - 2 \rangle$ RAs are marked with the white and black dots, respectively.

different energy routes such as absorption, reflection, and diffraction, it is being directed with very high efficiency (∼92%) to the zeroth-order transmission. Another observation from Figure 5d is the coincidence of the transmission dip and group delay dip. This is a typical behavior of resonances, which appears even for a single resonance without the coupling dynamics.[42] The negative group delay can be attributed to the fast light regions, though the associated high absorption prevents any practical use of it.[42]

2.5. The Role of the Interplay between Incident and Scattered Fields

To further investigate the origin of the transparency seen along the RAs we use the CDA to examine the electric fields at the array surface, that is, at the near field. The local field at the ith nanoparticle can be written as $E_{loc,i} = E_{inc,i} + E_{sca,i}$, where $E_{inc,i}$ and $E_{sca,i}$ are the incident field on the ith nanoparticle, and scattered fields from all the $j \neq i$ particles, respectively. The polarization of the ith nanoparticle can be written as $P_i = \alpha_s E_{loc,i}$ or alternatively, by

terms of α_{eff} obtained with the CDA as $P_i = \alpha_{eff} E_{inc,i}$. From the last three equations, the ratio of scattered to incident fields can be obtained

$$\frac{E_{sca,i}}{E_{inc,i}} = \frac{\alpha_{eff,i}}{\alpha_s} - 1 \qquad (2)$$

We would expect the scattered field to be influenced mainly by the coherent or incoherent sum of scattered fields from all the nanoparticles at the array, and by the nanoparticles' scattering amplitudes, reflected by α_s. In **Figure 6** we show the amplitude (Figure 6a) and phase (Figure 6b) of $E_{sca,i}/E_{inc,i}$. Several observations can be made from these figures. As seen in Figure 6a, along the RAs the scattered fields are substantially increased, reaching values of $|E_{sca,i}| \approx |E_{inc,i}|$ at the transparency regions. These strong scattered fields are the result of the coherent buildup of the scattered fields at the RAs condition. In addition, at the region of absorption bands (i) and (iii), there are also relatively strong incoherently scattered fields (typically $|E_{sca,i}| \approx 0.5|E_{inc,i}|$) getting their contribution from the plasmonic resonance of α_s. Absorption band (ii) shows similar order of

ADVANCED
SCIENCE NEWS

www.advancedsciencenews.com

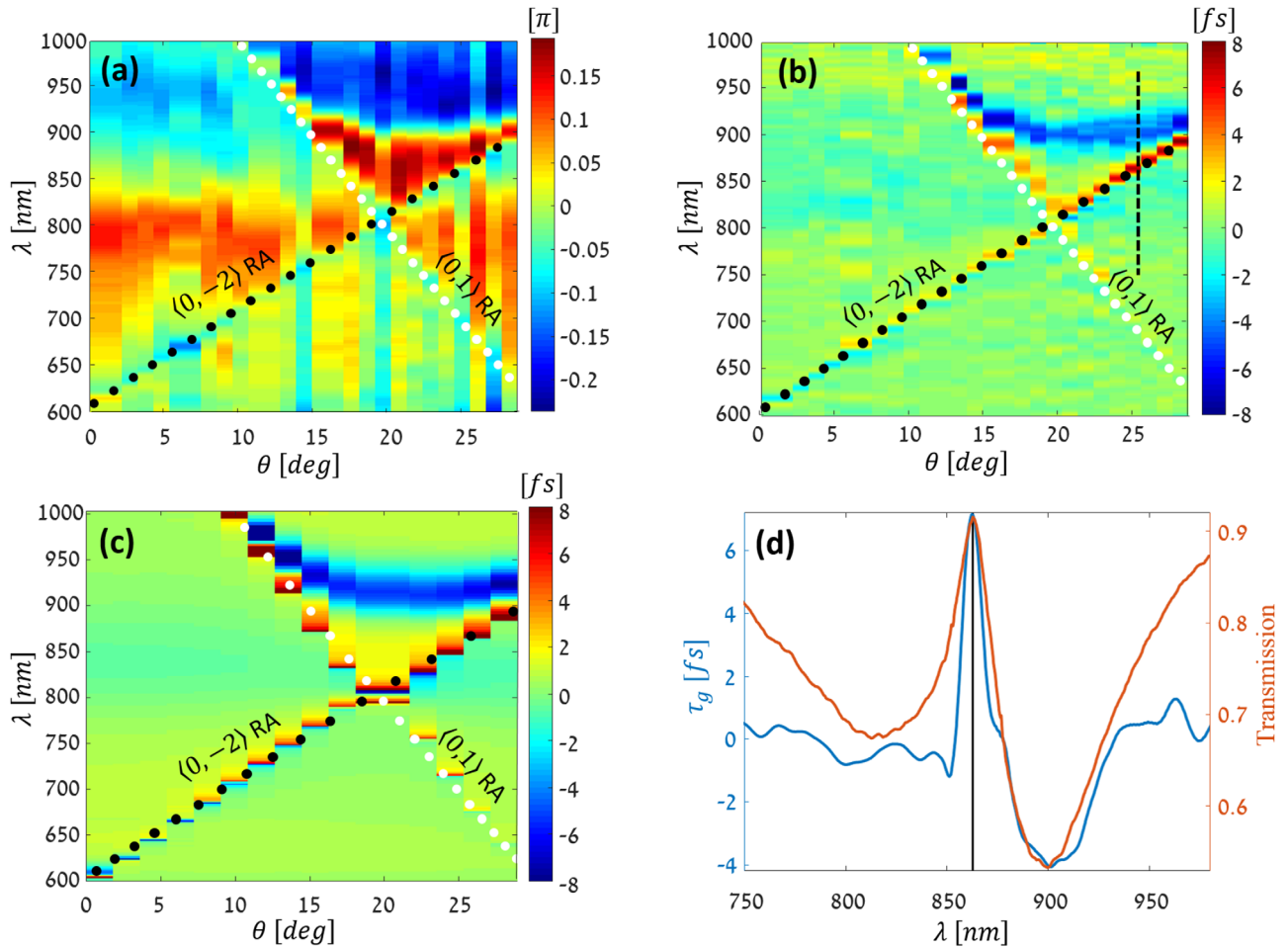LASER
& PHOTONICS
REVIEWS

www.lpr-journal.org

Figure 5. SLRs induced slow light. a) The *x*-polarized spectral phase for varying incident angles. b) Experimental and c) simulated by FDTD solver group delay calculated by $\tau_g = -\frac{d\phi}{d\omega}$. In (a–c) the $\langle 0, 1 \rangle$ and $\langle 0 - 2 \rangle$ RAs are marked with the white and black dots, respectively. d) A cross section of the group delay (blue) and the transmission (orange) for angle of 26°. The black vertical line corresponds to the $\langle 0 - 2 \rangle$ RA.
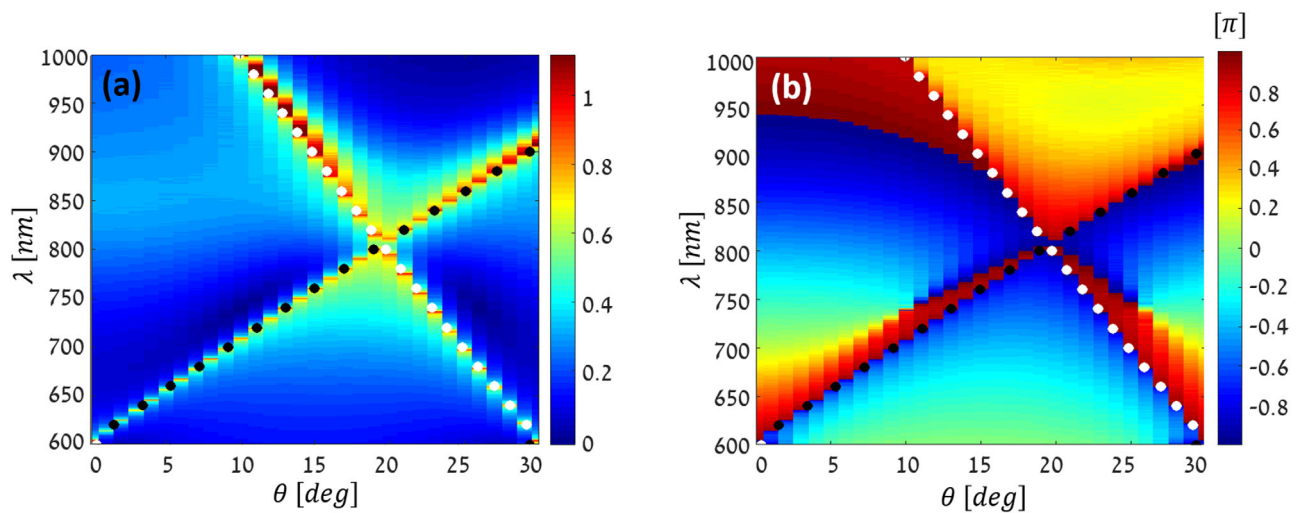

Figure 6. Calculated normalized scattered fields. a) Amplitude and b) phase of $E_{sca,i}/E_{app,i}$.

scattered fields, which in this case arise from the coupling of the plasmonic and photonic modes. From Figure 6b we see that along the RAs' transparency the scattered fields have a π-shifted phase relative to the incident field. Therefore, equal magnitudes and opposite phases of the scattered and incident fields cause complete destructive interference and thus give rise to the narrow transparency windows at the spectral coexistence of the plasmonic and photonic modes. Rearrangement of Equation (2) reflects how this destructive interference eliminates the effective polarizability: $\alpha_{\text{eff}} = \alpha_s(\frac{E_{\text{sca},i}}{E_{\text{inc},i}} + 1)$. If we set the condition reflected from Figures 6a,b of $E_{\text{sca},i}/E_{\text{inc},i} \approx -1$ we get $\alpha_{\text{eff}}^{(RAs)} \approx 0$, which agrees well with our experiment and simulations.

3. Conclusions

To conclude, we have demonstrated experimentally the existence of SLR induced transparency in plasmonic metasurfaces and its association with slow-light behavior. The plasmonic and photonic modes of the metasurface, respectively play the role of broad driven superradiant and narrow undriven subradiant coupled modes that are crucial to obtain EIT-like behavior. The effect is angle-dependent and can be tuned over a wide spectral range of ∼200 nm. At the transparency windows, the group delay of the light reaches values of ∼8 fs within only 40 nm thick sample. This corresponds to ∼60 times longer interaction with the sample than in the case of non-resonant interaction. These values, along with the high transmission values, can be further improved by optimizing the controllable parameters in the CDA with a figure of merit of high quality transparency and slow light window. Intriguingly, in the studied case, in a counter-intuitive manner, strong scattering at the LSPR promotes the long-range interaction, while their coherent buildup almost totally eliminates the absorption. The SLR induced transparency and slow-light effects supported by our metasurface occur for S polarization. Examining also the zero-order transmitted light from the sample at P polarization, shows that at the transparency regions no similar effects take place at P polarization (see Section S4, Supporting Information). This reassembles Brewster-angle-like behavior, though for S polarization instead for P polarization. The presented study opens the door for implementation in the fields of sensing, displays, polarizers, optical buffers, tunable filtering, and enhanced nonlinear interaction. In addition, we believe that this work will promote fundamental future studies of nonlocal coherent interaction in metamaterials to facilitate the route toward tunable, integrated, ultra-small slow-light devices with high delaying capabilities.

Supporting Information

Supporting Information is available from the Wiley Online Library or from the author.

Acknowledgements

Conflict of Interest

The authors declare no conflict of interest.

Keywords

[1] J. D. Joannopoulos, P. R. Villeneuve, S. Fan, *Nature* **1997**, *386*, 143.
[2] R. W. Boyd, *Nonlinear Optics*, 3rd ed., Academic Press, New York **2008**.
[3] L. Rayleigh, *Proc. R. Soc. A* **1907**, *79*, 399.
[4] V. G. Kravets, A. V. Kabashin, W. L. Barnes, A. N. Grigorenko, *Chem. Rev.* **2018**, *118*, 5912.
[5] W. Wang, M. Ramezani, A. I. Väkeväinen, P. Törmä, J. G. Rivas, T. W. Odom, *Mater. Today* **2018**, *21*, 303.
[6] B. B. Rajeeva, L. Lin, Y. Zheng, *Nano Res.* **2018**, *11*, 4423.
[7] T. K. Hakala, A. J. Moilanen, A. I. Väkeväinen, R. Guo, J.-P. Martikainen, K. S. Daskalakis, H. T. Rekola, A. Julku, P. Törmä, *Nat. Phys.* **2018**, *14*, 739.
[8] L. Michaeli, S. Keren-Zur, O. Avayu, H. Suchowski, T. Ellenbogen, *Phys. Rev. Lett.* **2017**, *118*, 243904.
[9] W. Zhou, M. Dridi, J. Y. Suh, C. H. Kim, D. T. Co, M. R. Wasielewski, G. C. Schatz, T. W. Odom, *Nat. Nanotechnol.* **2013**, *8*, 506.
[10] B. D. Thackray, V. G. Kravets, F. Schedin, G. Auton, P. A. Thomas, A. N. Grigorenko, *ACS Photonics* **2014**, *1*, 1116.
[11] M. Fleischhauer, A. Imamoglu, J. P. Marangos, *Rev. Mod. Phys.* **2005**, *77*, 633.
[12] N. Liu, L. Langguth, T. Weiss, J. Kästel, M. Fleischhauer, T. Pfau, H. Giessen, *Nat. Mater.* **2009**, *8*, 758.
[13] S. Zhang, D. A. Genov, Y. Wang, M. Liu, X. Zhang, *Phys. Rev. Lett.* **2008**, *101*, 47401.
[14] N. Papasimakis, V. A. Fedotov, N. I. Zheludev, S. L. Prosvirnin, *Phys. Rev. Lett.* **2008**, *101*, 253903.
[15] Y. Yang, I. I. Kravchenko, D. P. Briggs, J. Valentine, *Nat. Commun.* **2014**, *5*, 5753.
[16] R. D. Kekatpure, E. S. Barnard, W. Cai, M. L. Brongersma, *Phys. Rev. Lett.* **2010**, *104*, 243902.
[17] A. H. Safavi-Naeini, T. P. M. Alegre, J. Chan, M. Eichenfield, M. Winger, Q. Lin, J. T. Hill, D. E. Chang, O. Painter, *Nature* **2011**, *472*, 69.
[18] W. Cao, R. Singh, I. A. I. Al-Naib, M. He, A. J. Taylor, W. Zhang, *Opt. Lett.* **2012**, *37*, 3366.
[19] R. Singh, I. A. I. Al-Naib, Y. Yang, D. Roy Chowdhury, C. Cao, C. Rockstuhl, T. Ozaki, R. Morandotti, W. Zhang, *Appl. Phys. Lett.* **2011**, *99*, 201107.
[20] T. C. Tan, E. Plum, R. Singh, *Photonics* **2019**, *6*, 75.
[21] N. Liu, T. Weiss, M. Mesch, L. Langguth, U. Eigenthaler, M. Hirscher, C. Sönnichsen, H. Giessen, *Nano Lett.* **2010**, *10*, 1103.
[22] A. Artar, A. A. Yanik, H. Altug, *Nano Lett.* **2011**, *11*, 1685.

[23] M. Sandtke, L. Kuipers, *Nat. Photonics* **2007**, *1*, 573.

[24] A. Kocabas, S. S. Senlik, A. Aydinli, *Phys. Rev. Lett.* **2009**, *102*, 63901.

[25] K. Ooi, T. Okada, K. Tanaka, *Phys. Rev. B* **2011**, *84*, 115405.

[26] S. Linden, J. Kuhl, H. Giessen, *Phys. Rev. Lett.* **2001**, *86*, 4688.

[27] Z.-G. Dong, P.-G. Ni, J. Zhu, X. Zhang, *Opt. Express* **2012**, *20*, 7206.

[28] V. Yannopapas, E. Paspalakis, N. V. Vitanov, *Phys. Rev. B* **2009**, *80*, 35104.

[29] B. Tang, L. Dai, C. Jiang, *Phys. Lett. A* **2012**, *376*, 1234.

[30] X. Xiao, B. Zhou, X. Wang, J. He, B. Hou, Y. Zhang, W. Wen, *Sci. Rep.* **2015**, *5*, 12251.

[31] T. Zentgraf, S. Zhang, R. F. Oulton, X. Zhang, *Phys. Rev. B* **2009**, *80*, 195415.

[32] M. Manjappa, Y. K. Srivastava, R. Singh, *Phys. Rev. B* **2016**, *94*, 161103.

[33] M. C. Schaafsma, A. Bhattacharya, J. G. Rivas, J. Goez Rivas, *ACS Photonics* **2016**, *3*, 1596.

[34] T. C. Tan, Y. K. Srivastava, M. Manjappa, E. Plum, R. Singh, *Appl. Phys. Lett.* **2018**, *112*, 201111.

[35] S. Zou, N. Janel, G. C. Schatz, *J. Chem. Phys.* **2004**, *120*, 10871.

[36] S. Zou, G. C. Schatz, *J. Chem. Phys.* **2004**, *121*, 12606.

[37] B. Auguié, W. L. Barnes, *Phys. Rev. Lett.* **2008**, *101*, 143902.

[38] T. K. Hakala, H. T. Rekola, A. I. Väkeväinen, J.-P. Martikainen, M. Nečada, A. J. Moilanen, P. Törmä, *Nat. Commun.* **2017**, *8*, 13687.

[39] A. I. Väkeväinen, R. J. Moerland, H. T. Rekola, A. P. Eskelinen, J. P. Martikainen, D. H. Kim, P. Törmä, *Nano Lett.* **2014**, *14*, 1721.

[40] F. J. García de Abajo, *Rev. Mod. Phys.* **2007**, *79*, 1267.

[41] J. B. Khurgin, *Adv. Opt. Photonics* **2010**, *2*, 287.

[42] R. W. Boyd, *J. Mod. Opt.* **2009**, *56*, 1908.

[43] D. R. Smith, W. J. Padilla, D. C. Vier, S. C. Nemat-Nasser, S. Schultz, *Phys. Rev. Lett.* **2000**, *84*, 4184.

[44] R. A. Shelby, D. R. Smith, S. Schultz, *Science* **2001**, *292*, 77.

[45] S. Linden, C. Enkrich, M. Wegener, J. Zhou, T. Koschny, C. M. Soukoulis, *Science* **2004**, *306*, 1351.

[46] M. W. Klein, C. Enkrich, M. Wegener, S. Linden, *Science* **2006**, *313*, 502.

[47] N. Segal, S. Keren-Zur, N. Hendler, T. Ellenbogen, *Nat. Photonics* **2015**, *9*, 180.

[48] K. O'Brien, H. Suchowski, J. Rho, A. Salandrino, B. Kante, X. Yin, X. Zhang, K. OBrien, H. Suchowski, J. Rho, A. Salandrino, B. Kante, X. Yin, X. Zhang, K. O'Brien, H. Suchowski, J. Rho, A. Salandrino, B. Kante, X. Yin, X. Zhang, *Nat. Mater.* **2015**, *14*, 379.

[49] S. Keren-Zur, O. Avayu, L. Michaeli, T. Ellenbogen, *ACS Photonics* **2016**, *3*, 117.

[50] S. Keren-Zur, M. Tal, S. Fleischer, D. M. Mittleman, T. Ellenbogen, *Nat. Commun.* **2019**, *10*, 1778.

[51] I. De Leon, M. J. Horton, S. A. Schulz, J. Upham, P. Banzer, R. W. Boyd, *Sci. Rep.* **2015**, *5*, 13034.

[52] S. R. K. Rodriguez, A. Abass, B. Maes, O. T. A. Janssen, G. Vecchi, J. Gómez Rivas, *Phys. Rev. X* **2011**, *1*, 021019.

[53] L. Shi, T. K. Hakala, H. T. Rekola, J.-P. Martikainen, R. J. Moerland, P. Törmä, *Phys. Rev. Lett.* **2014**, *112*, 153002.